10,000 cycles (Fig. 3F). HR-STEM and EDX mapping of $Pt_{C-S}$ after stability cycling show a highly crystalline composite NP with an intact Pt shell and a well-alloyed TiWC core (Fig. 3F and fig. S21). We attribute the improved stability of the core-shell materials to the strong NM-TMC interfacial bonds and to the lower surface free energies of large NPs relative to the surface free energies of ultrasmall NPs. These results demonstrate the ability of our method to reformulate a classic bimetallic NM catalyst, such as PtRu, into an architecture that preserves the complexity of the original bimetallic surface chemistry while favorably modulating catalytic performance through subsurface strain and ligand effects. As a class of materials that breaks the traditional metal-adsorbate scaling relations for transition metals (32), TMCs not only serve as promising core candidates to reduce NM loadings but could favorably affect catalytic activity for industrially relevant reactions, such as HOR, MOR, water-gas shift, or methanol synthesis, in which CO coverage effects deeply influence catalyst performance.

The high-temperature self-assembly process used here permits comprehensive control of the entire core-shell architecture for a variety of early and late transition metals (Fig. 4). Using TiWC cores, we synthesized NPs of controlled sizes (3 to 10 nm) with mono- and bimetallic shell compositions using mixtures of Ru, Rh, Ir, Pt, and Au (Fig. 4A and figs. S22 to S24). All materials crystallized into fcc WC lattices and displayed enhanced surface NM:TiW ratios, consistent with core-shell structures (figs. S25 to S27 and table S5). In addition, NM shells lattice-matched and self-assembled onto bimetallic semicarbide cores (PDF no. 00-020-1315) such as $(Cu_{0.2}W_{0.8})_2C$, $(Co_{0.2}W_{0.8})_2C$, and $(Ni_{0.3}W_{0.7})_2C$ (Fig. 4, B and C, and figs. S28 and S29). Although NM interfacial bond formation and stability were not explored on all possible TMC core formulations, our data suggest broader applicability of the method for synthesizing a variety of NM/TMC combinations.

For Au, Pt, and PtAu monolayers self-assembled on TiWC cores, the RME method also allowed control of the NM shell thickness from submonolayer [~0.5 monolayer (ML)] to multilayer (~3 ML) coverages (Fig. 4D). For each material, the extent of the XPS-determined surface NM:TiW ratio enhancement over the ICP-determined bulk NM:TiW ratio correlated with the monolayer coverage, ranging from 1 to 3% at submonolayer coverages to 10 to 20% screening at multilayer coverages (table S5). Unlike Au surfaces, the surface of Pt passivates under ambient conditions with a PtO layer, which is detectable as $Pt^{2+}$ with XPS. As the monolayer coverage decreased for the Pt/TiWC system (Fig. 4D, spectra f to d), the Pt 4f signals shifted to higher binding energies, reaching 72.3 and 75.7 eV for the submonolayer sample (denoted as $Pt_{sub-ML}$). The presence of only PtO is consistent with submonolayer coverage, and such materials could have important applications in thermal catalysis, where both WC and Pt surface functionalities are accessible for catalytic transformations. When $Pt_{sub-ML}$ was supported on carbon and heated to 400° and 600°C

in different atmospheres ($H_2$, dry $N_2$, or $H_2O$-saturated $N_2$), neither sintering nor discrete fcc Pt crystallites were detectable when using TEM and PXRD, and an enriched Pt:W ratio showing only $Pt^{2+}$ surface species was observed with XPS (figs. S30 to S33). Collectively, TMC NPs coated with NM monolayers offer new, highly tunable pathways for decreasing NM loading requirements while increasing activity and stability in thermo- and electrocatalysis.

### REFERENCES AND NOTES

1. A. T. Bell, *Science* **299**, 1688–1691 (2003).
2. G. A. Deluga, J. R. Salge, L. D. Schmidt, X. E. Verykios, *Science* **303**, 993–997 (2004).
3. J. Zhang, K. Sasaki, E. Sutter, R. R. Adzic, *Science* **315**, 220–222 (2007).
4. Y. Zhai *et al.*, *Science* **329**, 1633–1636 (2010).
5. L. Zhang *et al.*, *Science* **349**, 412–416 (2015).
6. C. Chen *et al.*, *Science* **343**, 1339–1343 (2014).
7. J. Greeley *et al.*, *Nat. Chem.* **1**, 552–556 (2009).
8. P. Strasser *et al.*, *Nat. Chem.* **2**, 454–460 (2010).
9. H. Yang, *Angew. Chem. Int. Ed.* **50**, 2674–2676 (2011).
10. F. Tao *et al.*, *Science* **322**, 932–934 (2008).
11. S. Alayoglu, A. U. Nilekar, M. Mavrikakis, B. Eichhorn, *Nat. Mater.* **7**, 333–338 (2008).
12. C. S. Bonifacio *et al.*, *Chem. Mater.* **27**, 6960–6968 (2015).
13. C. Cui, L. Gan, M. Heggen, S. Rudi, P. Strasser, *Nat. Mater.* **12**, 765–771 (2013).
14. C. Wang *et al.*, *Adv. Funct. Mater.* **21**, 147–152 (2011).
15. D. V. Esposito, J. G. Chen, *Energy Environ. Sci.* **4**, 3900–3912 (2011).
16. I. E. Stephens, A. S. Bondarenko, U. Grønbjerg, J. Rossmeisl, I. Chorkendorff, *Energy Environ. Sci.* **5**, 6744–6762 (2012).
17. J. A. Schaidle, N. M. Schweitzer, O. T. Ajenifujah, L. T. Thompson, *J. Catal.* **289**, 210–217 (2012).
18. S. T. Oyama, *The Chemistry of Transition Metal Carbides and Nitrides* (Blackie, Glasgow, 1996).
19. S. Ono, T. Kikegawa, Y. Ohishi, *Solid State Commun.* **133**, 55–59 (2005).
20. R. B. Levy, M. Boudart, *Science* **181**, 547–549 (1973).
21. L. H. Bennett, J. R. Cuthill, A. J. McAlister, N. E. Erickson, R. E. Watson, *Science* **184**, 563–565 (1974).
22. D. V. Esposito, S. T. Hunt, Y. C. Kimmel, J. G. Chen, *J. Am. Chem. Soc.* **134**, 3025–3033 (2012).
23. T. G. Kelly, A. L. Stottlemyer, H. Ren, J. G. Chen, *J. Phys. Chem. C* **115**, 6644–6650 (2011).
24. S. T. Hunt, T. Nimmanwudipong, Y. Román-Leshkov, *Angew. Chem. Int. Ed.* **53**, 5131–5136 (2014).
25. See the supporting materials on *Science* Online.
26. Y. C. Kimmel, X. Xu, W. Yu, X. Yang, J. G. Chen, *ACS Catal.* **4**, 1558–1562 (2014).
27. W. Schottky, *Annal. Physik* **362**, 541–567 (1918).
28. B. Hammer, Y. Morikawa, J. K. Nørskov, *Phys. Rev. Lett.* **76**, 2141–2144 (1996).
29. Z. Liu, G. S. Jackson, B. W. Eichhorn, *Angew. Chem. Int. Ed.* **49**, 3173–3176 (2010).
30. T. J. Schmidt, H. A. Gasteiger, R. J. Behm, *Electrochem. Commun.* **1**, 1–4 (1999).
31. A. K. Singh, Q. Xu, *ChemCatChem* **5**, 652–676 (2013).
32. R. Michalsky, Y. J. Zhang, A. J. Medford, A. A. Peterson, *J. Phys. Chem. C* **118**, 13026–13034 (2014).

---

## ROBOTICS

# Perching and takeoff of a robotic insect on overhangs using switchable electrostatic adhesion

M. A. Graule,[1,2]* P. Chirarattananon,[2,3] S. B. Fuller,[2,4] N. T. Jafferis,[2] K. Y. Ma,[2] M. Spenko,[5] R. Kornbluh,[6] R. J. Wood[2]*

For aerial robots, maintaining a high vantage point for an extended time is crucial in many applications. However, available on-board power and mechanical fatigue constrain their flight time, especially for smaller, battery-powered aircraft. Perching on elevated structures is a biologically inspired approach to overcome these limitations. Previous perching robots have required specific material properties for the landing sites, such as surface asperities for spines, or ferromagnetism. We describe a switchable electroadhesive that enables controlled perching and detachment on nearly any material while requiring approximately three orders of magnitude less power than required to sustain flight. These electroadhesives are designed, characterized, and used to demonstrate a flying robotic insect able to robustly perch on a wide range of materials, including glass, wood, and a natural leaf.

**M**icro aerial vehicles (MAVs) with the capability to stay aloft for a prolonged time would be invaluable in many applications: providing a bird's-eye view of a disaster area, detecting hazardous chemical or biological agents, or enabling secure signal transmission in ad hoc communication networks. However, the flight time of aerial robots is restricted by the weight of their on-board power supplies and the lifetime of their mechanical components. Moreover, the endurance of current aerial robots decreases substantially as vehicle scale
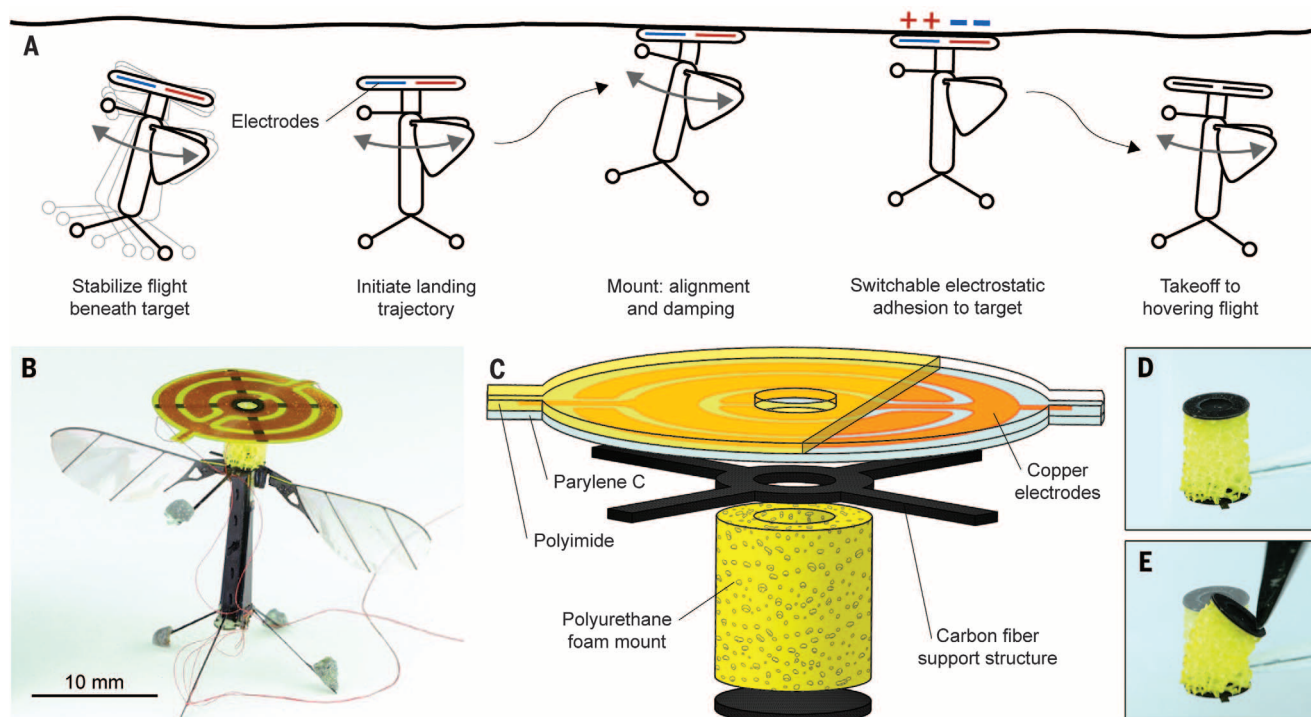
**Fig. 1. Robot design and principle of operation.** (**A**) Before initiating a perching maneuver, the robot attains stable hovering underneath the target surface. A compliant mount assures successful alignment between the adhesive patch and the target surface. Upon contact, the electrodes in the patch induce surface charges on the substrate, leading to an electrostatic attraction between the surface and the patch. These surface charges recombine when the voltage between the electrodes is switched off, allowing for a smooth detachment. (**B**) Depiction of the flapping wing MAV capable of landing on and relaunching from the underside of nearly any material. (**C**) The adhesion mechanism relies on compliant circular copper electrodes on a polyimide film that are embedded in Parylene C to generate electrostatic adhesion. This is supported by a carbon fiber cross and integrated with the robot through a polyurethane foam mount. The final version of the mechanism weighs 13.4 mg (robot without payload, 84mg). (**D** and **E**) The polyurethane foam mount provides damping and passive alignment to facilitate perching over a wide envelope of trajectories and allows us to integrate features to assist with characterizing the flight performance before perching experiments (fig. S11).

diminishes (*1*). Perching—defined in this case to mean alighting onto a surface or object and remaining attached—on commonly available overhangs such as trees, buildings, or powerlines would allow MAVs to continue their mission while conserving energy, thus expanding their mission time. Hanging underneath these structures would provide a clear path to the ground for vision or signal transmission and protection from extreme weather conditions.

Whereas birds, bats, and insects are capable of perching on compliant and wind-buffeted surfaces such as tree branches, leaves, and flowers (*2–4*), it has proven challenging to reproduce this aerial prowess to dynamically land MAVs on and relaunch from a broad range of natural and artificial targets. Demonstrations to date predominantly focus on bird-sized vehicles. Proposed

approaches include a passive biomimetic gripper (*5*), directional dry adhesives in a spring-lever system (*6*), magnets with servo-actuated release (*7*), an articulated nondirectional dry adhesive that is repositioned when perching is desired (*8*), and microspines (*9*) or needles (*10*) driven into a soft target by a preloaded snapping mechanism. Perching and relaunch with a high success rate was achieved on rough walls with microspines that engage in surface asperities, which can be released through resistively heating a shape-memory alloy actuator (*11*). Additionally, advanced control strategies were developed for fixed-wing MAVs to land on specific targets via a high angle-of-attack stalling maneuver (*12*) or transitioning into hovering flight (*13*).

Insect-like aerial robots may exceed the agility of larger systems at lower costs, but their deployment comes with a number of additional challenges. For example, perching with articulated and actuated mechanisms becomes impractical at insect scales because of challenges in manufacturing and the destabilizing effect of asymmetrically moving parts on vehicle dynamics. Chemical adhesives may not require complex mechanisms for attachment but are either irreversible, require pressure for engagement, or cause destabilizing torques during detachment (*8*, *14*). An alternative is the use of electrostatic adhesives, which have been used in mechanically simple, low-power attachment mechanisms across

a broad range of substrates (*15*, *16*) and were successfully implemented in decimeter-scale climbing robots for vertical walls (*17–20*). Although recent advances have combined this form of adhesion with gecko-inspired dry adhesives for improved performance over a variety of substrates (*21*), electroadhesives are not typically as strong as, for example, pressure-sensitive or thermoplastic adhesives (*22*). However, because a robot's surface area–to–volume ratio increases with decreasing size, electroadhesion becomes increasingly promising for smaller devices, and its electrical and mechanical simplicity make it particularly attractive for insect-sized vehicles.

We leveraged these prior insights regarding electrostatic adhesion and propose a controllable attachment principle for small-scale MAV perching. Our method enables repeatable transitions from flight to perching, as well as transitions from attachment to stable hovering flight on overhanging surfaces consisting of wood, glass, or a natural leaf (Fig. 1A) with a tethered insect-scale flapping wing robot (Fig. 1B) (*23*). The method relies on the electrostatic force between interdigitated circular electrodes (voltage difference, 1000 V) (Fig. 1C) and the opposing surface charges they induce on the target substrate. The electrodes are integrated with the robot through a foam mount, which provides damping and passive alignment so as to ensure reliable attachment for a broad range of landing

[1]Department of Mechanical Engineering, Massachusetts Institute of Technology, Cambridge, MA 02139, USA. [2]John A. Paulson School of Engineering and Applied Sciences and the Wyss Institute for Biologically Inspired Engineering, Harvard University, Cambridge, MA 02138, USA. [3]Department of Mechanical and Biomedical Engineering, City University of Hong Kong, Kowloon, Hong Kong. [4]Department of Mechanical Engineering, University of Washington, Seattle, WA 98195, USA. [5]Mechanical, Materials, and Aerospace Engineering Department, Illinois Institute of Technology, Chicago, IL 60616, USA. [6]SRI International, Menlo Park, CA 94025, USA.
*Corresponding author. Email: graule@mit.edu (M.A.G.); rjwood@seas.harvard.edu (R.J.W.)
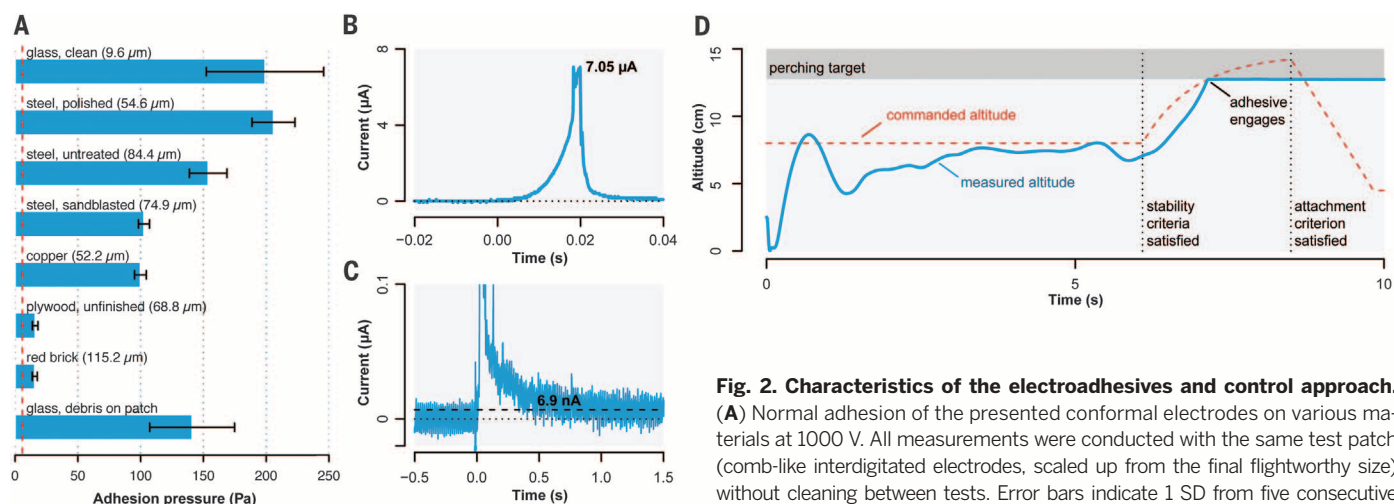
**Fig. 2. Characteristics of the electroadhesives and control approach.** (**A**) Normal adhesion of the presented conformal electrodes on various materials at 1000 V. All measurements were conducted with the same test patch (comb-like interdigitated electrodes, scaled up from the final flightworthy size) without cleaning between tests. Error bars indicate 1 SD from five consecutive measurements. For each substrate, the arithmetic mean of the absolute values of the surface asperities is stated in parentheses. The dashed red line indicates the pressure required to support the vehicle weight (including the adhesion mechanism), assuming a patch size as used in our demonstrations. (**B**) Charging current for the circular patch on glass at 1000 V [switched on at time (*t*) = 0 s]. Charging requires 37.7 µJ on glass, 37.4 µJ on wood, and 46.6 µJ on copper. (**C**) Current in the charging phase and during steady state on glass (1000 V). A leakage current of 6.9 nA occurs on glass (1.4 nA on wood; 1.0 nA on copper). The mechanism requires 6.9 µW to remain perched on glass (1.4 µW on wood; 1.0 µW on copper). This is substantially lower than the flight power of 19 mW (*23*). (**D**) Commanded and measured altitude during an exemplary perching flight. The logic module initiates a bio-inspired landing trajectory once the robot has achieved stable hovering in the target region underneath the substrate. The flapping amplitude is ramped down (corresponding to a decrease in commanded altitude) once the logic module detects a successful attachment.
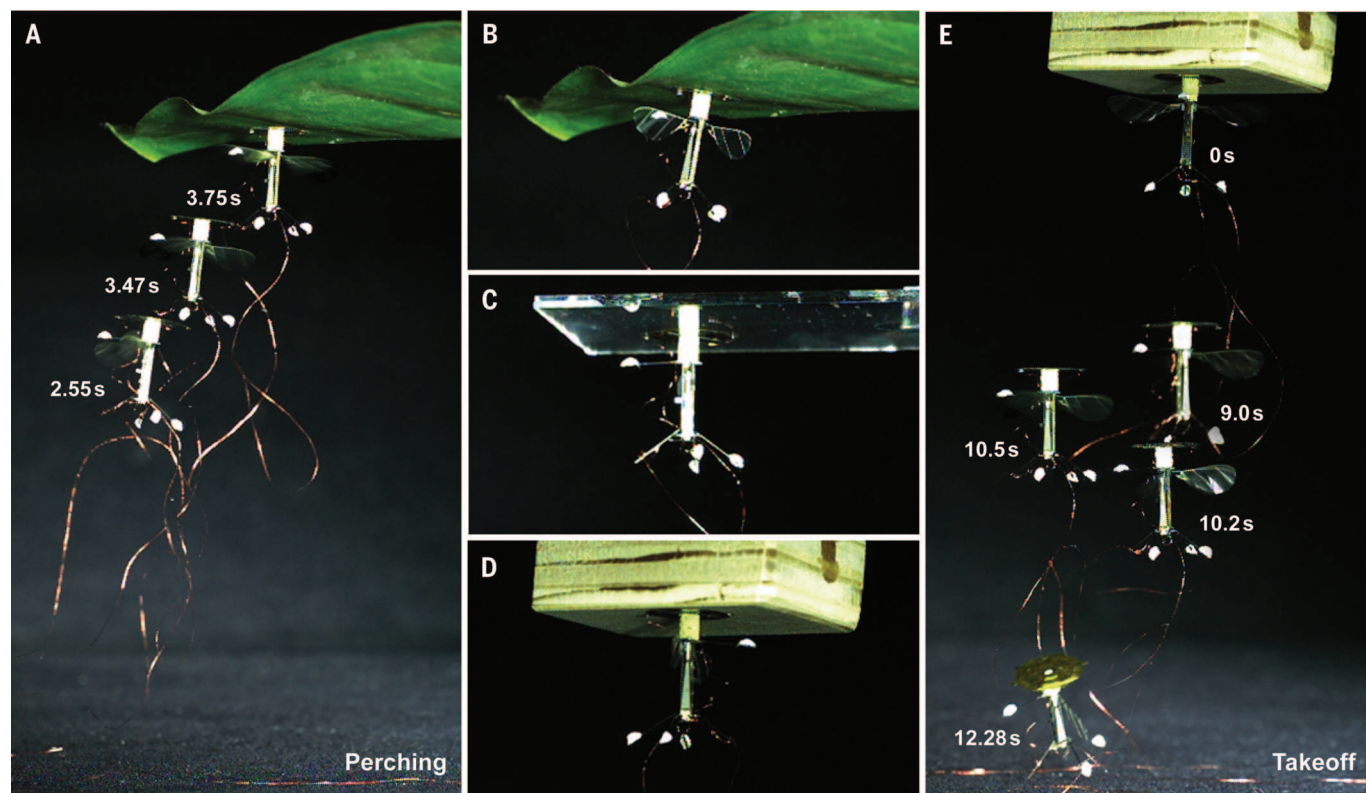


**Fig. 3. Perching and relaunch demonstrations on a leaf, glass, and unfinished plywood.** (**A**) Frame overlay from a high-speed video taken of a successful landing maneuver on a natural leaf. (**B** to **D**) The micro aerial vehicle after successfully landing on a leaf, glass, and unfinished plywood (wings turned off). (**E**) Frame overlay from a high-speed video taken of a successful relaunch from unfinished wood, followed by stable hovering flight (10.5 s) and a smooth landing on the ground (12.28 s).

trajectories. We further demonstrate torque-free detachment from unfinished wood through de-energizing the patch, followed by stable hovering flights (Fig. 1A). The electroadhesive patch and the compliant mount provide a lightweight (13.4 mg, less than 15% of the total body mass) and physically simple mechanism for effective perching.

Electrostatic adhesives were fabricated by embedding ~200-nm-thick interdigitated copper electrodes (fig. S1) between thin polymer layers so as to produce compliant adhesive patches with a high adhesion pressure per weight [fabrication details are provided in fig. S2 and (*24*)]. When placed on a target substrate with a voltage across the electrodes, the patch induces areas of net

charge on the surface of the substrate. These charges mirror the charges accumulated in the electroadhesive patch, leading to an attractive force between the patch and the substrate. This force increases with decreasing thicknesses of the insulating layer and the air gap at the interface (and thus is inversely related to the surface roughness), increases with increasing applied voltage (19, 25), and is affected by humidity [detailed discussion is available in (24), section 2.4.2], material properties, leakage currents, and non-uniform charge distribution on the interface (19, 25). The strong dependence on environmental parameters for this type of adhesive makes it challenging to accurately predict the attractive forces analytically or numerically (24).

We therefore pursued an experimental approach to characterize the normal adhesion pressures and guide the final design of our electrode patch [exact geometries are provided in fig. S3; experimental details are provided in (24), section 2.4, and fig. S4]. Electroadhesive patches with comb-like interdigitated electrodes (fig. S3) were created and tested on glass, steel (with varying surface texture), copper, unfinished plywood, and red brick. To appropriately mimic multiple attach/detach cycles as expected under normal use, the test patch was not cleaned between measurements. It therefore attracted both debris from the substrates and airborne particles over time. Tests on glass were performed at the start and end of the substrate test series in order to illustrate the effect of accumulated debris on the adhesion performance.

When activated at 1000 V, the test patch provided a normal adhesion pressure of at least 15.6 Pa on all the investigated substrates at 59 to 70% relative humidity. The repeated measurements on glass showed that the achievable adhesion pressure drops by <30% after 35 attachment/release iterations across different materials and 6 hours of exposure to airborne debris without cleaning (Fig. 2A). The normal pressure shows a high variance, which can be explained by its dependence on environmental parameters, such as the alignment of the patch with the target surface, the presence of debris or surface irregularities, and relative humidity [an analysis of surface roughness is available in (24), section 2.4, and figs. S5 and S6, and a discussion on humidity is available in fig. S7].

These experiments show that sufficient adhesion can be achieved with 1000 V, and this voltage was chosen for the final demonstrations. Although a higher voltage could provide greater adhesion, practical issues—such as the breakdown strength of the power wires used in flight experiments, or the feasibility of onboard high-voltage electronics on a future prototype—favor choosing lower voltages (24). At a minimal adhesion pressure of 15.6 Pa, a patch area of 0.63 cm$^2$ would be required to carry the weight of the microrobot (total weight, ~100 mg; robot, 84 mg; patch and glue, ~16 mg). The size of the final patch was chosen to be 1.7 cm$^2$ in order to accommodate for the uncertainty in actual adhesion pressure caused by relative humidity, naturally rough or dirty surfaces,

and degradation that will occur upon repeated attach and detach cycles. This patch was fabricated in the same manner as the larger test patch but relies on circular interdigitated electrodes to promote symmetric normal and shear forces, thus reducing the risk of destabilizing torques from residual charges during takeoff maneuvers (from a perched state). Simulated adhesion pressures are comparable for the two geometries [(24), section 2.2, and table S1]. We determined the charging and leakage current of the circular patch at 1000 V on glass, wood, and copper, finding that the power it requires to maintain the robot attached (<7 μW) is at least three orders of magnitude lower than the flight power of 19 mW required by our vehicle (Fig. 2, B and C, and fig. S8) (24).

Our control strategy for perching is inspired by the finding that honeybees hold the apparent rate of image expansion constant during a perching maneuver, which translates to an approach speed that is linear in the distance to the target (26). To realize a linearly decreasing approach speed, we implemented a controller that sets the reference height so that the distance to the target decays exponentially. In order to enable high reliability in the attachment maneuvers, the landing sequence is initiated only after the robot achieves a predefined stability metric (position and orientation errors and linear and angular velocities below specified thresholds) while hovering at a desired position underneath the perching target. The controller architecture relies on a logic module that detects relevant events such as stable hovering or a successful attachment. This module adjusts the reference position to initiate the perching and detachment maneuvers and ramps down the flapping amplitude once the landing is completed. The reference position is then fed into two adaptive controller blocks, one controlling altitude, the other controlling attitude and latitude (23). The system relies on position and orientation feedback from a motion-tracking arena to close the control loop (fig. S9). The functionality of the logic module is illustrated with data from an exemplary landing maneuver in Fig. 2D.

The fast dynamics of the underactuated microrobot, its inherent instability, and its susceptibility to disturbances (such as wind gusts), particularly in close proximity to the attachment point, render the precise tracking of a reference trajectory challenging. For example, we found that the lift of our flapping-wing vehicle increases by >40% in close proximity to ceilings (fig. S10). To address this, a tube-shaped, laser-cut polyurethane foam damper (chosen for its low density and low coefficient of restitution) was used to mount the patch onto the robot. This passive mechanism reduces the chance of rebound during high-velocity collisions and provides passive alignment between the patch and the perching target. This promotes successful attachments over a broad envelope of landing trajectories.

This combination of lightweight conformal electrodes with a flexible, energy-absorbing mount enabled reliable perching on a wide range of natural and artificial overhangs. We demonstrated this capability by executing subsequent transitions from free flight to stable attachment on a leaf (two

perching attempts), glass (one perching attempt), and unfinished plywood (three perching attempts), as well as two takeoffs into hovering flight from wood (Fig. 3 and movie S1). One of the perching attempts on the leaf failed because the leaf occluded the robot from the motion capture system, causing an emergency shut-off of the actuation before alignment with the target was achieved [(24), section 2.5]. The other five attempts were successful.

Given the limited payload capacities and the energetically expensive nature of flight at small scales, perching presents an opportunity to increase mission durations, and hence utility, of MAVs. Deploying insect-like MAVs presents substantial challenges in manufacturing, actuation, sensing, power, and control. However, a decrease in scale does not only come with challenges, but also offers new capabilities. Motivated by the increased dominance of area-dependent forces at reduced sizes, we have demonstrated that electrostatic adhesives are an attractive option to achieve robust and dynamic perching behavior in an insect-like robot. The techniques for developing and integrating compliant electroadhesives may also find utility in other small-scale robotics tasks such as delicate micromanipulation and adhesion for inclined and inverted terrestrial locomotion.

**REFERENCES AND NOTES**

1. D. Floreano, R. J. Wood, *Nature* **521**, 460–466 (2015).
2. M. Tschapka, *Biol. J. Linn. Soc. Lond.* **80**, 281–288 (2003).
3. B. Anderson, W. W. Cole, S. C. H. Barrett, *Nature* **435**, 41–42 (2005).
4. M. Sazima, I. Sazima, *Can. J. Zool.* **77**, 47–51 (1999).
5. C. E. Doyle *et al.*, *IEEE/ASME Trans. Mechatron.* **18**, 506–517 (2013).
6. E. W. Hawkes *et al.*, "Dynamic surface grasping with directional adhesion," 2013 IEEE/RSJ International Conference on Intelligent Robots and Systems (IROS), pp. 5487–5493 (2013).
7. J. F. Roberts, J. C. Zufferey, D. Floreano, "Energy management for indoor hovering robots," 2008 IEEE/RSJ International Conference on Intelligent Robots and Systems (IROS), vols 1–3, Conference Proceedings, pp. 1242–1247 (2008).
8. L. Daler, A. Klaptocz, A. Briod, M. Sitti, D. Floreano, "A perching mechanism for flying robots using a fibre-based adhesive," 2013 IEEE International Conference on Robotics and Automation (ICRA), pp. 4433-4438 (2013).
9. D. Mellinger, M. Shomin, V. Kumar, Control of quadrotors for robust perching and landing. *Proc. Int. Power. Lift Conf.* **2010**, 205–225 (2010).
10. M. Kovač, J. Germann, C. Hürzeler, R. Y. Siegwart, D. Floreano, *J. Micro-Nano Mech.* **5**, 77–91 (2009).
11. A. Lussier Desbiens, A. Asbeck, M. Cutkosky, *Int. J. Robot. Res.* **30**, 355–370 (2011).
12. R. Cory, R. Tedrake, Experiments in fixed-wing UAV perching. *Proc. AIAA Guid. Nav. Contr. Conf.* **2008**, 1–12 (2008).
13. A. Frank, J. McGrew, M. Valenti, D. Levine, J. P. How, *Hover, Transition, and Level Flight Control Design for a Single-Propeller Indoor Airplane* (Defense Technical Information Center, 2007).
14. M. L. Anderson *et al.*, "The sticky-pad plane and other innovative concepts for perching uavs," 47th AIAA Aerospace Sciences Meeting (2009).
15. G. J. Monkman, *Int. J. Robot. Res.* **16**, 1–10 (1997).
16. J. P. D. Téllez, J. Krahn, C. Menon, "Characterization of electro-adhesives for robotic applications," 2011 IEEE International Conference on Robotics and Biomimetics (ROBIO), pp. 1867–1872 (2011).
17. H. Prahlad, R. Pelrine, S. Stanford, J. Marlow, R. Kornbluh, "Electroadhesive robots—Wall climbing robots enabled by a novel, robust, and electrically controllable adhesion technology," 2008 IEEE International Conference on Robotics and Automation (ICRA), pp. 3028–3033 (2008).
18. R. Liu, R. Chen, H. Shen, R. Zhang, *Int. J. Adv. Robot. Syst.* **10**, 36 (2013).
19. R. Chen, R. Liu, H. Shen, "Modeling and analysis of electric field and electrostatic adhesion force generated by interdigital electrodes for wall climbing robots," 2013 IEEE/RSJ

International Conference on Intelligent Robots and Systems (IROS), pp. 2327–2332 (2013).

20. H. Wang, A. Yamamoto, T. Higuchi, "Electrostatic-motor-driven electroadhesive robot," 2012 IEEE/RSJ International Conference on Intelligent Robots and Systems (IROS), pp. 914–919 (2012).
21. D. Ruffatto 3rd, A. Parness, M. Spenko, *J. R. Soc. Interface* **11**, 20131089 (2014).
22. L. Wang, L. Graber, F. Iida, *IEEE Trans. Robot.* **29**, 863–874 (2013).
23. K. Y. Ma, P. Chirarattananon, S. B. Fuller, R. J. Wood, *Science* **340**, 603–607 (2013).
24. Materials and methods are avialable as supplementary materials on *Science* Online.
25. M. R. Sogard, A. R. Mikkelson, M. Nataraju, K. T. Turner, R. L. Engelstad, *J. Vac. Sci. Technol. B* **25**, 2155–2161 (2007).
26. E. Baird, N. Boeddeker, M. R. Ibbotson, M. V. Srinivasan, *Proc. Natl. Acad. Sci. U.S.A.* **110**, 18686–18691 (2013).

## SYNAPSE FORMATION

# Control of neuronal synapse specification by a highly dedicated alternative splicing program

Lisa Traunmüller,* Andrea M. Gomez,* Thi-Minh Nguyen, Peter Scheiffele†

Alternative RNA splicing represents a central mechanism for expanding the coding power of genomes. Individual RNA-binding proteins can control alternative splicing choices in hundreds of RNA transcripts, thereby tuning amounts and functions of large numbers of cellular proteins. We found that the RNA-binding protein SLM2 is essential for functional specification of glutamatergic synapses in the mouse hippocampus. Genome-wide mapping revealed a markedly selective SLM2-dependent splicing program primarily consisting of only a few target messenger RNAs that encode synaptic proteins. Genetic correction of a single SLM2-dependent target exon in the synaptic recognition molecule neurexin-1 was sufficient to rescue synaptic plasticity and behavioral defects in *Slm2* knockout mice. These findings uncover a highly selective alternative splicing program that specifies synaptic properties in the central nervous system.

Alternative splicing provides a key mechanism for neuron-specific gene expression (*1–3*). An array of RNA-binding proteins broadly expressed in neuronal cells has been implicated in controlling developmentally regulated and neuron-specific alternative splicing programs, with single proteins regulating hundreds of target transcripts (*4–6*). However, some RNA-binding proteins are selectively expressed in neuronal populations, raising the possibility that they may control cell type– and synapse-specific functions (*7, 8*).

The KH-domain RNA-binding protein SLM2 is highly expressed in glutamatergic pyramidal cells of the mouse hippocampus and in a specific subset of γ-aminobutyric acid (GABA)–releasing interneurons (*9, 10*). In *Slm2*$^{KO}$ knockout (KO) mice, glutamatergic spine synapses formed at normal numbers on the primary apical dendrites of hippocampal CA1 neurons (Fig. 1, A and B). Western blot analysis of synaptosome fractions from wild-type (WT) and *Slm2*$^{KO}$ hippocampi revealed overall normal concentrations of glutamatergic synapse proteins. However, there was an increase in the AMPA-type glutamate receptor (AMPAR) subunit GluA1, in particular in

Biozentrum, University of Basel Klingelbergstrasse 50-70, 4056 Basel, Switzerland
*These authors contributed equally to this work. †Corresponding author. Email: peter.scheiffele@unibas.ch

detergent-soluble fractions from adult *Slm2*$^{KO}$ mouse synaptosomes (Fig. 1, C and D). In acute slices from adolescent mice (postnatal day 25), GluA1 amounts were elevated in total cell lysates and cell surface fractions, whereas *N*-methyl-ᴅ-aspartate (NMDA)–receptor GluN1 subunit expression was unaltered (Fig. 1, E and F). Whole-cell voltage-clamp recordings from CA1 neurons in *Slm2*$^{KO}$ hippocampal slices showed no difference in the miniature excitatory postsynaptic current (mEPSC) amplitude and frequency between WT and *Slm2*$^{KO}$ mice (Fig. 2, A and B). However, mEPSC events showed a modest increase in the speed of rise and decay times in *Slm2*$^{KO}$ CA1 neurons (Fig. 2, C and D). AMPAR/NMDAR ratios were significantly increased in *Slm2*$^{KO}$ mice (Fig. 2, E and F). In *Slm2*$^{KO}$ CA1 neurons, stimulation of Schaffer collaterals elicited larger postsynaptic responses as compared to WT (Fig. 2G; see also fig. S1A for data from field EPSP recordings). Paired-pulse facilitation was normal in *Slm2*$^{KO}$ (Fig. 2H). In sum, these experiments demonstrate an elevation in postsynaptic AMPAR surface expression and function in CA1 neurons of *Slm2*$^{KO}$ mice. Finally, long-term potentiation (LTP) induced by theta-burst stimulation of Schaffer collaterals was significantly reduced in acute slices from *Slm2*$^{KO}$ mice (Fig. 2I).

Candidate gene approaches have identified some transcripts that are altered in *Slm2*$^{KO}$ brains (*9–12*). However, a comprehensive global analysis of SLM2 targets is lacking. Using Illumina paired-end sequencing we mapped SLM2-dependent alternative splicing events at a genome-wide level. This analysis revealed highly correlated expression of transcripts between genotypes, indicating that SLM2 does not play a major role in tuning overall transcript levels (Fig. 3A). Moreover, transcripts encoding ionotropic and metabotropic glutamate receptors were not significantly changed (fig. S1, B to E). Most significantly altered was the transcript encoding the SLM2 paralogue SLM1, which has previously been shown to be up-regulated in *Slm2*$^{KO}$ hippocampus (*11*).

Genome-wide splicing patterns were extracted on the basis of annotations from FAST DB, and splicing indices calculated. The vast majority of exons remained essentially unchanged between WT and *Slm2*$^{KO}$ hippocampi (Fig. 3B and fig. S2A; analysis includes 4,965 microexons). Notably, alternative exons in four genes showed disproportionately strong deregulation in the *Slm2*$^{KO}$ hippocampus. There was a >2-fold increase in the incorporation of exons at the alternatively spliced segment four (AS4) of the neurexins (*Nrxn1, 2,* and *3*), three genes that encode synaptic cell surface receptors. Moreover, exon 24 incorporation was 1.58-fold elevated in tomosyn-2 (*Stxbp5l*), a component of the vesicle fusion machinery. Another seven exons were identified that exhibited significant alterations (*P* < 0.01) although with modest fold-change (Fig. 3C and table S1). Independent experimental validation confirmed that deregulation of additional candidate target exons was small or in some cases not detectable (Fig. 3, D and E, and fig. S2B). The paralogue SLM1 may compensate for the loss of SLM2 (*11*). However, comparison of candidate exons in *Slm1*$^{KO}$, *Slm2*$^{KO}$, and *Slm1:Slm2*$^{DKO}$ (double knockout) mice revealed that deregulation was not significantly more severe in the DKO mice (fig. S2C).

Alternative splicing at *Nrxn* AS4 regulates selective trans-synaptic interactions of neurexins in the presynaptic terminal with several synaptic receptors (*13–16*). For an unbiased identification of interaction partners regulated by this alternative splicing event, we performed affinity purifications on recombinant NRX1β4(+) and NRX1β4(−) isoforms, followed by shot-gun mass spectrometry (Fig. 4A and fig. S3, A and B). We identified 21 candidate binding partners, including known neurexin-binding proteins (Cbln2, the leucine-rich repeat proteins LRRTM1,2,4, neuroligin-1,2, 3, and the sortilin-related VPS10-domain containing receptor

# Science

## Perching and takeoff of a robotic insect on overhangs using switchable electrostatic adhesion

M. A. Graule, P. Chirarattananon, S. B. Fuller, N. T. Jafferis, K. Y. Ma, M. Spenko, R. Kornbluh and R. J. Wood

**Making small robots stick**
Aerial views offer the chance to observe a wide range of terrain at once, but they come at the cost of needing to stay aloft. Graule *et al.* found that electrostatic forces could keep their insect-sized flying robot stuck to the underside of a range of surfaces (see the Perspective by Kovac). They mounted an electrostatically charged pad to the top of their r obot, which could then reversibly stick to existing elevated perches—including a leaf—using less power than would be needed for sustained flight.
*Science*, this issue p. 978; see also p. 895

| | |
|---|---|
| ARTICLE TOOLS | http://science.sciencemag.org/content/352/6288/978 |
| SUPPLEMENTARY MATERIALS | http://science.sciencemag.org/content/suppl/2016/05/18/352.6288.978.DC1 |
| RELATED CONTENT | http://science.sciencemag.org/content/sci/352/6288/895.full<br>file:/content |
| REFERENCES | This article cites 19 articles, 2 of which you can access for free<br>http://science.sciencemag.org/content/352/6288/978#BIBL |
| PERMISSIONS | http://www.sciencemag.org/help/reprints-and-permissions |